

# Precision Meson Spectroscopy at COMPASS

B. Grube<sup>a</sup> for the COMPASS Collaboration

Excellence Cluster Universe, Technische Universität München, Boltzmannstr. 2, 85748 Garching, Germany.

**Abstract.** We present first results of a partial wave analysis of the diffractive reaction  $\pi^- \text{Pb} \rightarrow \pi^- \pi^+ \pi^- \text{Pb}$  based on data from the COMPASS experiment taken during a pilot run in 2004 using a 190 GeV/c  $\pi^-$  beam on a lead target. The analysis was performed in the region of squared four-momentum transfer  $t'$  between 0.1 and 1.0 (GeV/c)<sup>2</sup>. The  $\pi^- \pi^+ \pi^-$  final state shows a rich spectrum of well-known resonances. In addition a spin-exotic  $J^{PC} = 1^{-+}$  state with significant intensity was observed at 1.66 GeV/c<sup>2</sup> in the  $\rho(770)\pi$  decay channel in natural parity exchange. The resonant nature of this state is manifest in the mass dependence of its phase difference to  $J^{PC} = 1^{++}$  and  $2^{-+}$  waves. The measured resonance parameters are consistent with the disputed  $\pi_1(1600)$ . An outlook on the analyses of the much larger data set taken during 2008 and 2009 is given.

## 1 Introduction

The naïve Constituent Quark Model (CQM) describes light mesons as bound color-singlet states of quarks and anti-quarks with flavors  $u$ ,  $d$ , and  $s$  grouped into  $\text{SU}(3)_{\text{flavor}}$  multiplets. In the CQM the spin  $J$ , parity  $P$ , and charge conjugation  $C$  of a meson are given by

$$(1) \quad J = |L - S|, \dots, L + S; \quad P = (-1)^{L+1} \quad \text{and} \quad C = (-1)^{L+S}$$

where  $L$  is the relative orbital angular momentum of quark and antiquark and  $S = 0, 1$  the total intrinsic spin of the  $q\bar{q}'$  pair. In addition a meson is characterized by its isospin  $I$  and  $G$ -parity which is defined as

$$(2) \quad G = (-1)^{I+L+S}$$

Both quantum numbers are conserved in strong interactions.

Despite of its simplicity, the CQM works surprisingly well and explains a good part of the observed light meson spectrum as well as some of the meson properties, although it does not make any assumptions about the nature of the binding force. Quantum ChromoDynamics (QCD) describes the strong interaction between colored quarks by the exchange of gluons, which are colored themselves. Even though it is still not clear, how the confinement of quarks and gluons into hadrons is generated by the QCD Lagrangian, its structure suggests that there are color-singlet states beyond  $|q\bar{q}'\rangle$ . In particular one expects gluonic degrees of freedom, that reflect the non-Abelian character of QCD, to manifest themselves in the meson spectrum. Mesonic states beyond the CQM are classified into hybrids, glueballs, and multi-quark states [1]. Hybrids are  $|q\bar{q}'g\rangle$  resonances with constituent glue that contributes to the quantum numbers of the hadron. The  $q\bar{q}'$  pair is in a color-octet configuration which is neutralized in color by

the excited gluon. Glueballs are pure gluonic bound states  $|gg\rangle$ . Multi-quark states include tetraquarks and mesonic molecules. Most of these states will be hardly distinguishable from ordinary  $|q\bar{q}'\rangle$  states with the same  $J^{PC}$  and will mix with them so that physically observable states are in general a linear combination of  $|q\bar{q}'\rangle$  and additional basis states that is experimentally very difficult to disentangle. An unambiguous evidence for the existence of mesonic states beyond the CQM, as allowed by QCD, would be the discovery of exotic states with quantum numbers forbidden in the simple quark model. In the light-meson sector so-called spin-exotic states with quantum numbers  $J^{PC} = 0^{-+}, 0^{+-}, 1^{-+}, 2^{+-}, 3^{-+}, 4^{+-}, \dots$  are a particularly promising field of research.

In lattice QCD [2] simulations the lightest glueball is predicted to have ordinary scalar quantum numbers  $J^{PC} = 0^{++}$  and a mass of about 1.7 GeV/c<sup>2</sup>. A possible experimental glueball candidate is the  $f_0(1500)$  seen by the Crystal Barrel [3] and WA102 [4] experiments. The interpretation of the data is, however, complicated by the mixing of the  $f_0(1500)$  with other states.

The lowest mass hybrid, on the other hand, is predicted [5] to have exotic quantum numbers  $J^{PC} = 1^{-+}$  so that it will not mix with ordinary resonances. It is expected to have a mass between 1.3 and 2.2 GeV/c<sup>2</sup> and in the flux-tube model it preferentially decays into  $b_1(1235)\pi$  and  $f_1(1285)\pi$  [6]. Three experimental candidates for isovector spin-exotic  $J^{PC} = 1^{-+}$  states were found so far: The  $\pi_1(1400)$  was seen in  $\pi^- N \rightarrow \pi^- \eta N$  by the E852 [7] and VES [8] experiments. Crystal Barrel observed a  $1^{-+} \eta\pi$  state in  $\bar{p}n \rightarrow \pi^- \pi^0 \eta$  [9] and  $\bar{p}p \rightarrow \pi^0 \pi^0 \eta$  [10] Dalitz plot analyses. Another  $1^{-+}$  state, the  $\pi_1(1600)$ , was seen at higher mass by the E852 and VES experiments in  $\rho\pi$  [11,12,13],  $\eta'\pi$  [14,15],  $f_1\pi$  [16,17], and  $b_1\pi$  [18,17] decay modes in peripheral  $\pi^- p$  interactions. It was also reported in  $\bar{p}p \rightarrow b_1\pi\pi$  [19]. The resonant nature of both  $1^{-+}$  states is still discussed controversially in the commu-

<sup>a</sup> e-mail: bgrube@ph.tum.de

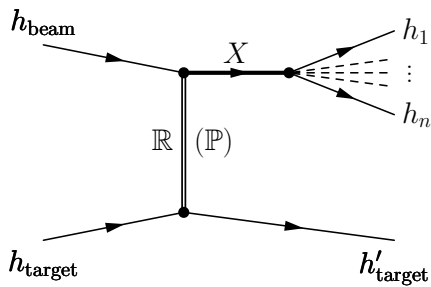


**Fig. 1.** Production of resonance  $X$  in diffractive scattering of the beam particle  $h_{\text{beam}}$  off the target particle  $h_{\text{target}}$  and its subsequent decay into  $n$  hadrons  $h_1, \dots, h_n$ . The interaction is mediated by exchange of a Reggeon  $\mathbb{R}$  and leaves target particle intact. At high energies the Pomeron  $\mathbb{P}$  is the dominant Regge-trajectory.

nity [8,17]. In particular the observation of the  $\pi_1(1600)$  in the  $\rho\pi$  decay channel is heavily disputed. A different analysis of a larger E852 data set showed that an extension of the wave set, used to model the data, makes the  $\pi_1(1600)$  signal disappear [20]. A third  $1^{-+}$  state, the  $\pi_1(2000)$ , was seen only by the E852 experiment in the  $f_1\pi$  [16] and  $b_1\pi$  [18] decay channel.

The COMPASS experiment sets out to settle these and other issues in light-meson spectroscopy by studying meson production in diffractive and central production reactions using high-energetic hadron beams on various fixed targets.

Diffractive reactions are known to exhibit a rich spectrum of produced states. In diffractive meson production the target particle remains intact and interacts with the incident beam particle via  $t$ -channel Reggeon exchange. In this process the beam particle  $h_{\text{beam}}$  is excited to some resonance  $X$  which then dissociates into the final state as illustrated in Fig. 1:

$$(3) \quad h_{\text{beam}} + h_{\text{target}} \rightarrow X + h'_{\text{target}} \quad \text{and} \quad X \rightarrow h_1 + \dots + h_n$$

The process can be characterized by two kinematic variables: the square of the total center-of-mass energy,  $s = (p_{\text{beam}} + p_{\text{target}})^2$ , and the squared four-momentum transfer from the incoming beam particle to the outgoing system  $X$ ,  $t = (p_{\text{beam}} - p_X)^2$ . It is custom practice to use the variable  $t' = |t| - |t|_{\text{min}}$  instead of  $t$ , where  $|t|_{\text{min}}$  is the minimum value of  $|t|$  allowed by kinematics for a given  $X$  invariant mass  $m_X$ . The value of  $|t|_{\text{min}}$  is small but larger than zero, because of the additional longitudinal four-momentum transfer which is required by  $m_X > m_{\text{beam}}$ . At high beam energies the diffraction is dominated by Pomeron exchange [21] so that isospin and  $G$ -parity of the intermediate state  $X$  are the same as that of the beam particle. In addition the final state particles are produced mostly at small angles with respect to the beam direction which requires a high angular resolution and coverage of the detector.

In central production reactions the mesonic state is produced in Reggeon-Reggeon fusion, where both beam and target particle remain unaltered. This is illustrated in Fig. 2. These reactions will enhance scalar mesons and in particular to the  $f_0(1500)$ . It is also believed that in central

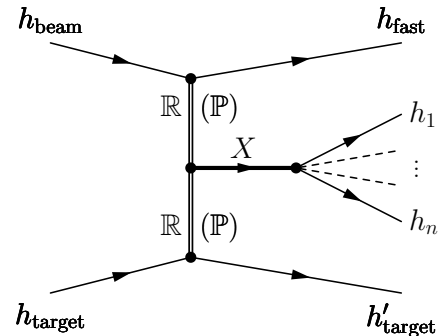


**Fig. 2.** Central production of meson  $X$  in Reggeon-Reggeon fusion and its subsequent decay into  $n$  hadrons  $h_1, \dots, h_n$ . Both beam and target particles stay intact.

production gluonic degrees of freedom are enriched which makes it a promising reaction for glueball searches. The produced resonance  $X$  carries only a small fraction  $x_F \approx 0$  of the maximum possible longitudinal momentum  $p_L^{\text{max}}$  in the center-of-mass frame, where  $x_F = p_L/p_L^{\text{max}} \approx 2p_L/\sqrt{s}$ . The scattered beam hadron has  $x_F \approx 1$  and the target  $x_F \approx -1$ . In fixed target geometry this means that the scattered beam particle appears as the leading hadron  $h_{\text{fast}}$  in the event, while the target recoil proton is slow. The centrally produced system is separated from the leading hadron and the recoil particle by rapidity gaps.

## 2 Experimental Setup

Finding mesonic states that do not fit into the CQM in the light-quark sector is an experimentally challenging task. There is a high density of broad overlapping states so that the signal can only be extracted from interference effects. This requires large data sets and a complete phase space coverage of the experiment. The COMMon Muon and Proton Apparatus for Structure and Spectroscopy (COMPASS) [22] is a fixed-target experiment at the CERN Super Proton Synchrotron (SPS) and is well suited for this task: It is a two-stage spectrometer built to measure at high beam intensities. The detector covers a wide range of scattering angles and particle momenta and has a high angular resolution. In the target region scintillating fibers and planes of silicon microstrip detectors are used for beam definition and vertexing. The setup has two large dipole magnets with 1.0 and 5.5 Tm bending power which both are surrounded by staggered tracking detectors with increasing granularity and resolution towards the beam axis. The two spectrometer stages are equipped with hadronic and electromagnetic calorimeters. This enables COMPASS to reconstruct final states with charged as well as neutral particles like  $\pi^0$ ,  $\eta$ , and  $\eta'$ . In addition the first stage features a Ring Imaging Cherenkov (RICH) detector able to separate charged final state pions and kaons in the momentum range between 5 and 50 GeV/c.

The M2 beamline that feeds the COMPASS experiment is very versatile and can deliver high-intensity sec-

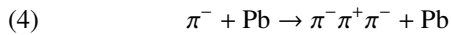
ondary hadron as well as polarized tertiary muon beams which are produced at a production target by the incoming 400 GeV/c proton beam from the SPS. The hadron beams can have a momentum of up to 300 GeV/c and a maximum intensity of  $4 \cdot 10^7 \text{ sec}^{-1}$ . The positive hadron beam consists of 71.5 %  $p$ , 25.5 %  $\pi^+$ , and 3.0 %  $K^+$ , the negative beam has 96.0 %  $\pi^-$  and 3.5 %  $K^-$ .

The suitability of the COMPASS setup for meson spectroscopy was studied in a short pilot run in 2004, where a 190 GeV/c  $\pi^-$  beam was shot onto a fixed lead target. Based on the experience from this run the spectrometer was upgraded in order to address the challenges of the hadron spectroscopy physics program. A Recoil Proton Detector (RPD) was installed around a 40 cm long liquid hydrogen target. The RPD measures the time-of-flight of the recoil protons using two barrels of scintillator slats and provides information for the trigger decision. The read-out electronics of the electromagnetic calorimeters was upgraded and the central part of the second calorimeter was equipped with 800 radiation-hard Shashlik blocks. In addition the tracking close to the beam axis and the vertex definition were improved by adding high-resolution Pixel-GEM detectors in the spectrometer and cryogenic silicon microstrip detectors in the target region, respectively. At the same time the material budget in the beam region was reduced. Also the particle identification capabilities were enhanced by utilizing the RICH detector in the first spectrometer stage and two ChErenkov Differential counters with Achromatic Ring focus (CEDAR) upstream of the target which are able to identify the incoming beam particles.

With this enhanced setup COMPASS took diffractive and central production data in 2008 and 2009 using 190 GeV/c negative and positive hadron beams on liquid hydrogen, nickel, tungsten, and lead targets. The goal of collecting about ten times the available world statistics for both production reactions has been achieved.

### 3 Diffractive Production of $\pi^- \pi^+ \pi^-$

During the 2004 pilot run COMPASS was able to record within a few days a data sample of the diffractive reaction



with competitive statistics using a 190 GeV/c  $\pi^-$  beam on a total 3 mm thick lead target. The  $\pi^- \pi^+ \pi^-$  final state was chosen for a first analysis [23,24,25], because the controversial spin-exotic  $\pi_1(1600)$  has been observed in this channel.

#### 3.1 Data Sample and Event Selection

The trigger for diffractive events selected one incoming and at least two outgoing charged particles. In 2004 it consisted of several components. Incoming beam particles were selected by a coincidence of two scintillator discs with 5 cm diameter that were positioned upstream of the target and centered about the beam axis. A veto system with

a 4 cm central hole rejected beam particles that were not crossing the target material. Additional lead-scintillator veto counters placed downstream of the target suppressed events with outgoing particles that were emitted under large angles so that they would fall out of the acceptance. A system of three scintillation detectors in the spectrometer, so-called beam killers, vetoed non-interacting beam particles. In order to enrich diffractive events, a scintillator disk with 5 cm diameter was placed after the target and was used as a multiplicity counter, selecting events with at least two forward charged particles. In addition at least one cluster with minimum energy deposit of 6 GeV was required in the hadronic calorimeter in the second spectrometer stage.

The 2004 data sample contains about  $87.7 \cdot 10^6$  events from the diffractive trigger which were subject to further offline event selection. Events were required to have exactly one primary vertex with one incoming beam and three outgoing charged tracks. The primary vertex position was constraint to the target region and the three outgoing tracks were required to have a charge sum of  $-1$ . Diffractive events were enriched by an exclusivity cut. However, the spectrometer setup was not able to measure the energy of the incident beam particle event-by-event, only the direction of the beam particle and thus the scattering angle  $\theta$  was determined precisely by a silicon microstrip beam telescope. In the 2004 setup also the target recoil particle was not detected. For small momentum transfer, large beam energy, and assuming specific target and recoil masses the beam energy  $E_{\text{beam}}$  and the momentum transfer  $t'$  can be calculated in good approximation from the well-measured quantities  $m_X$ ,  $E_X$ , and  $\theta$ . For the analysis the  $t'$  region between 0.1 and 1.0  $(\text{GeV}/c)^2$  was selected, where the  $\pi_1(1600)$  was reported in the past. In this  $t'$  region the beam particles were assumed to scatter off quasi-free nucleons inside the Pb nuclei of the target. The validity of this assumption is supported by the roughly exponential falling  $t'$ -spectrum shown in Fig. 3 which has a slope parameter compatible with the nucleon radius. Exclusive  $\pi^- \pi^+ \pi^-$  production was selected by requiring the reconstructed beam

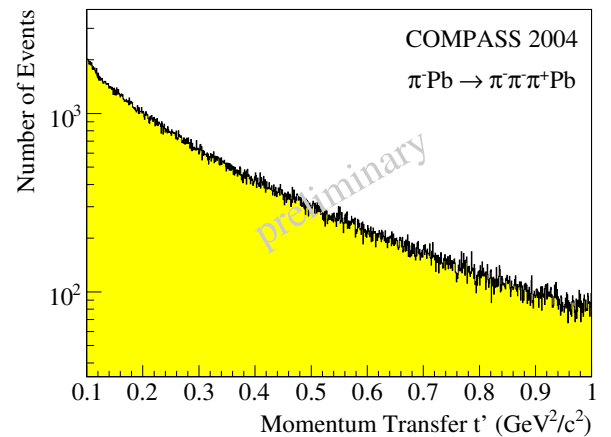


**Fig. 3.** Spectrum of the squared four-momentum transfer  $t' = |t| - |t|_{\text{min}}$  in logarithmic scale. The data exhibit a roughly exponential behavior.

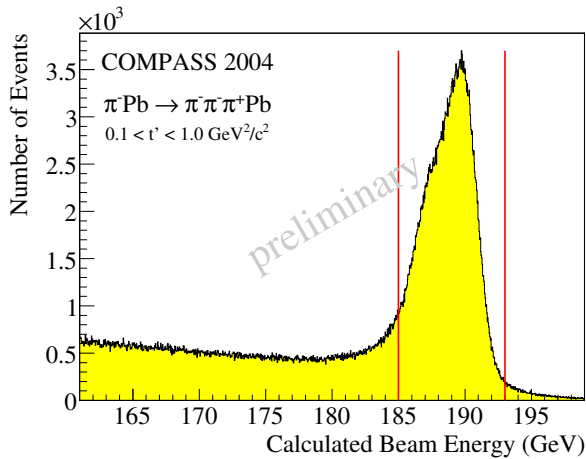


**Fig. 4.** Distribution of the beam energy  $E_{\text{beam}}$  calculated from  $m_X$ ,  $E_X$ , and  $\theta$  for the  $t'$  range between 0.1 and 1.0  $(\text{GeV}/c)^2$ . The exclusivity cut is indicated by the vertical lines.

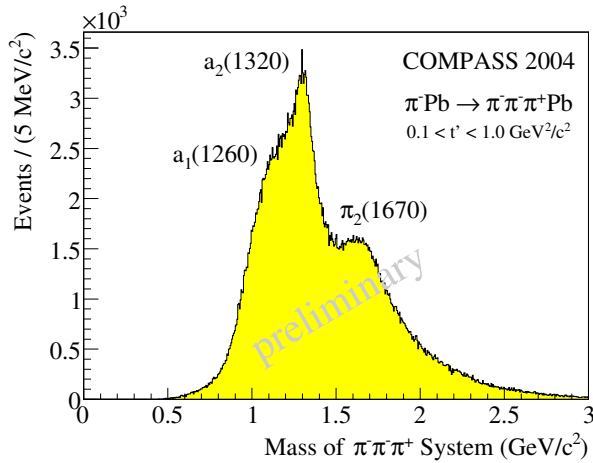


**Fig. 5.**  $\pi^- \pi^+ \pi^-$  invariant mass distribution of the selected data sample for  $t' \in [0.1, 1.0]$   $(\text{GeV}/c)^2$ .

energy  $E_{\text{beam}}$  to be maximum 4 GeV off the mean beam energy of 189 GeV (see Fig. 4). About 420 000 events in the mass range between 0.5 and 2.5  $\text{GeV}/c^2$  pass all of the above selection cuts.

In the 2004 pilot run there was no particle identification for the incoming beam particles. The non-pionic component of the beam of about 5 % consists mainly of  $K^-$ . Their decays and diffractive reactions constitute part of the background in the analysis. Also for the final state no particle identification was applied.

### 3.2 Partial-Wave Analysis

Figure 5 shows the  $\pi^- \pi^+ \pi^-$  invariant mass distribution of the selected data sample. It exhibits clear structures in the mass region of the well-known resonances  $a_1(1260)$ ,  $a_2(1320)$ , and  $\pi_2(1670)$ . In order to find and disentangle the various resonances in the data, a partial-wave analysis (PWA) was performed.

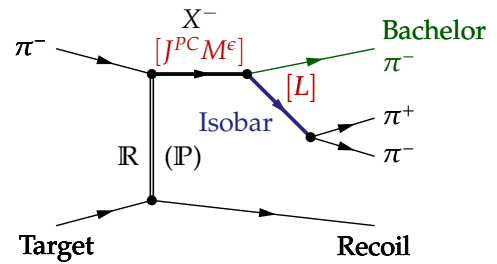


**Fig. 6.** A partial wave in the isobar model. The diffractively produced  $X^-$  with quantum numbers  $J^{PC} M^\epsilon$  decays first into an isobar and a bachelon  $\pi^-$ . The isobar has spin  $S$  and a relative orbital angular momentum  $L$  with respect to the  $\pi^-_{\text{bachelor}}$ . The isobar then decays in a second step into  $\pi^+ \pi^-$ .

The PWA employed in this analysis is based on two basic assumptions. We assume that the total cross section factorizes into a resonance and a recoil vertex and we use the isobar model to describe the  $X^-$  decay. This by definition neglects any final state interaction of the outgoing pions or the isobar with the target as well as within the  $\pi^- \pi^+ \pi^-$  system. The isobar model decomposes the decay  $X^- \rightarrow \pi^- \pi^+ \pi^-$  into a chain of successive two-body decays: First the  $X^-$  with quantum numbers  $J^{PC}$  decays into a dipion resonance, the so-called isobar, and a bachelon pion  $\pi^-_{\text{bachelor}}$ . The isobar has spin  $S$  and a relative orbital angular momentum  $L$  with respect to  $\pi^-_{\text{bachelor}}$ .  $L$  and  $S$  couple to the  $X^-$  spin  $J$ . Second the isobar decays into  $\pi^+ \pi^-$ . This is illustrated in Fig. 6. In general the  $\pi^- \pi^+ \pi^-$  system has isospin  $I \geq 1$ . Since there are no known flavor-exotic light-quark mesons and Pomeron exchange is assumed, we set  $I = 1$ . A state with odd number of pions has negative  $G$ -parity so that the value of the charge conjugation  $C$  is fixed by  $G = C(-1)^I$  to be positive.

The spin-density matrix  $\rho_{i,i'}^\epsilon$  is parameterized in terms of production amplitudes  $V_{ir}^\epsilon$ :

$$(5) \quad \rho_{i,i'}^\epsilon = \sum_r^{N_r} V_{ir}^\epsilon V_{i'r}^{\epsilon*}$$

where  $i = J^{PC} M^\epsilon [\text{decay}] L$  and  $\epsilon$  denote a particular partial-wave amplitude that is characterized by the isobar state, the decay orbital angular momentum  $L$ , the spin quantum numbers  $J^{PC}$  of the  $X^-$  state, and by the spin projection  $M^\epsilon$  of  $J$ . The amplitudes are constructed in the reflectivity basis [26], where  $M \geq 0$  and where the reflectivity  $\epsilon = \pm 1$  describes the symmetry under reflection through the production plane. This basis is convenient, because, due to  $P$  parity conservation, amplitudes with different reflectivities do not interfere. Furthermore at high center-of-mass energies  $\sqrt{s}$  the reflectivity corresponds to the naturality of the exchanged Reggeon. The rank  $N_r$  of the spin density matrix is set to two to account for the helicity flip and non-flip amplitudes at the baryon vertex assuming that the target nucleon stays intact.

The observed intensity is parameterized as a coherent and incoherent sum over the partial-wave amplitudes [26]:

$$(6) \quad I(\tau; m_X) = \eta(\tau) \sum_{\epsilon=\pm 1} \sum_r^{N_r} \left| \sum_i^{\text{waves}} V_{ir}^\epsilon \psi_i^\epsilon(\tau; m_X) \right|^2$$

Here  $\tau$  represents the five phase space coordinates that completely describe the three-body kinematics. They are measured for each event and are used to calculate the decay amplitudes  $\psi_i^\epsilon$  which are constructed using non-relativistic Zemach tensors [27,28] and do not contain any free parameters. The decay of the  $X^-$  is described in its rest system using the Gottfried-Jackson frame [29] with the  $z$ -axis along the beam particle direction and the  $y$ -axis perpendicular to the production plane spanned by the beam and the recoil particle. The angular distribution of the isobar decay is defined in the canonical system obtained by pure Lorentz boost to the isobars rest frame. The production amplitudes  $V_{ir}^\epsilon$  are complex numbers that are determined from extended maximum likelihood fits to the data performed in  $40 \text{ MeV}/c^2$  wide bins in the three-pion invariant mass  $m_X$  using a program that was originally developed at Illinois [30] and later developed at Protvino and Munich. This so-called ‘‘mass-independent’’ fit takes into account the overall acceptance  $\eta$  as a function of the phase space variables. It does not include any parameterization of the produced resonances  $X^-$  and assumes constant production strengths of the waves within the  $m_X$  bin. The  $t'$  dependence of the wave intensities was implemented by multiplying the amplitudes with different  $t'$ -dependent functions of the form  $f_i^\epsilon(t') \propto e^{-bt'}$  for  $M = 0$  and  $f_i^\epsilon(t') \propto t' e^{-bt'}$  for  $M = 1$ , where the slope parameter  $b$  was determined from the data by fitting  $t'$  slices.

The acceptance was estimated using a Monte Carlo simulation. Events were generated uniformly according to three-body phase space with beam kinematics and  $t'$  distribution taken from the real data and then processed through the detailed detector simulation and the full reconstruction and event selection chain. Figure 7 shows that COMPASS has an excellent acceptance of more than 50 % for  $\pi^-\pi^+\pi^-$  final states even in the region  $m_X > 2 \text{ GeV}/c^2$ . Moreover the acceptance shows only weak dependence on the polar angle of the isobar in the Gottfried-Jackson frame (cf. Fig. 8). This is important for the PWA, since in [20] it was shown that a drop of the acceptance towards  $\cos \theta_{GJ} = \pm 1$  in combinations with detector resolution effects may lead to significant leakage of intensity between waves.

The PWA model includes five  $\pi^+\pi^-$  isobars [12]: The amplitudes of the  $\rho(770)$ ,  $f_2(1270)$ , and  $\rho_3(1690)$  were described using relativistic Breit-Wigner line shape functions including Blatt-Weisskopf barrier penetration factors [31]. The  $\pi^+\pi^- S$ -wave is in general dominated by a broad  $f_0(600)$  meson, a narrow  $f_0(980)$ , and several resonances above  $1 \text{ GeV}/c^2$ . We use the parameterization from [33] which is based on the ‘‘M’’ solution from Au, Morgan, and Pennington [34], but with the  $f_0(980)$  subtracted from the elastic  $\pi\pi$  amplitude and added as a separate Breit-Wigner resonance.

Due to the angular momentum carried by the Pomeron that is exchanged in diffractive reactions, the incoming  $\pi^-$

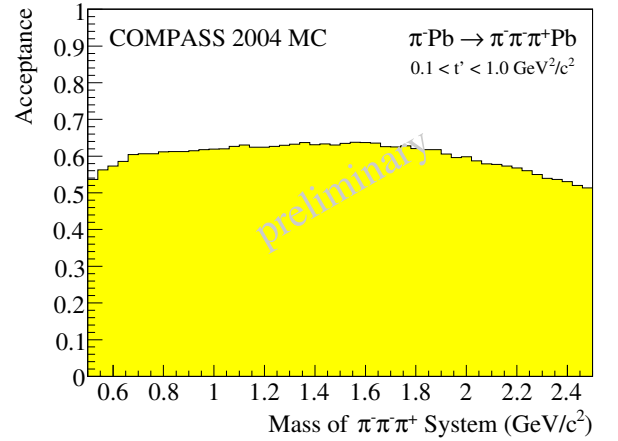


Fig. 7. Overall acceptance as a function of the  $\pi^-\pi^+\pi^-$  invariant mass  $m_X$ .

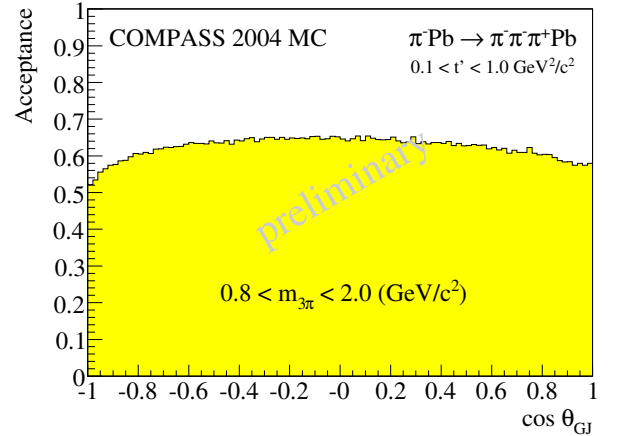


Fig. 8. Overall acceptance as a function of the cosine of the polar angle  $\theta_{GJ}$  of the isobar in the Gottfried-Jackson rest frame of the  $X^-$ .

( $J^P = 0^-$ ) can be excited to a state  $X^-$  with different  $J^P$ , which is limited only by the conservation laws of strong interaction. In the construction of the PWA model waves with  $J \leq 4$  and  $M \leq 1$  were considered. The final wave set of the model consists of 41 partial waves plus one incoherent isotropic background wave, the so-called ‘‘flat’’ wave. Table 1 lists all waves. Mostly positive reflectivity waves, corresponding to natural parity exchange production, are needed to describe the data. The wave set in particular includes the  $2^{-+}0^+[\rho\pi]F$ ,  $2^{-+}1^+[\rho\pi]F$ , and  $2^{-+}1^+[\rho\pi]P$  waves that in [20] were found to be crucial for describing the data and in addition made the exotic  $\pi_1(1600)$  signal disappear. Some of the waves have  $m_X$  thresholds below which their intensity was fixed to zero.

To ensure that the mass-independent fit found the global maximum of the likelihood, up to 100 independent fits were performed for each mass bin using random start parameters. Out of these fits the one with the largest likelihood was selected. In case two or more fits have ambiguous solutions that differ by less than one unit of likelihood, the

error of this bin was increased by the maximum difference of the solutions, which in the plots is indicated by thick green bars.

After performing the mass-independent fit the mass dependence of the production amplitudes of a subset of six waves (printed in boldface in Table 1) was fit in the range from 0.80 to 2.32 GeV/c<sup>2</sup> to a model parameterized in

**Table 1.** Wave set used for the mass-independent fit. The set consists of mostly positive reflectivity waves that correspond to natural parity exchange. The six waves printed in boldface are used in the mass-dependent fit.

| $J^{PC}$              | $M^\epsilon$         | $L$                   | Isobar $\pi$                | Threshold [GeV/c <sup>2</sup> ] |
|-----------------------|----------------------|-----------------------|-----------------------------|---------------------------------|
| 0 <sup>-+</sup>       | 0 <sup>+</sup>       | $S$                   | $(\pi\pi)_{S\pi}$           | —                               |
| <b>0<sup>-+</sup></b> | <b>0<sup>+</sup></b> | <b><math>S</math></b> | <b><math>f_0\pi</math></b>  | <b>1.400</b>                    |
| 0 <sup>-+</sup>       | 0 <sup>+</sup>       | $P$                   | $\rho\pi$                   | —                               |
| <b>1<sup>-+</sup></b> | <b>1<sup>+</sup></b> | <b><math>P</math></b> | <b><math>\rho\pi</math></b> | <b>—</b>                        |
| <b>1<sup>++</sup></b> | <b>0<sup>+</sup></b> | <b><math>S</math></b> | <b><math>\rho\pi</math></b> | <b>—</b>                        |
| 1 <sup>++</sup>       | 0 <sup>+</sup>       | $P$                   | $f_2\pi$                    | 1.200                           |
| 1 <sup>++</sup>       | 0 <sup>+</sup>       | $P$                   | $(\pi\pi)_{S\pi}$           | 0.840                           |
| 1 <sup>++</sup>       | 0 <sup>+</sup>       | $D$                   | $\rho\pi$                   | 1.300                           |
| 1 <sup>++</sup>       | 1 <sup>+</sup>       | $S$                   | $\rho\pi$                   | —                               |
| 1 <sup>++</sup>       | 1 <sup>+</sup>       | $P$                   | $f_2\pi$                    | 1.400                           |
| 1 <sup>++</sup>       | 1 <sup>+</sup>       | $P$                   | $(\pi\pi)_{S\pi}$           | 1.400                           |
| 1 <sup>++</sup>       | 1 <sup>+</sup>       | $D$                   | $\rho\pi$                   | 1.400                           |
| <b>2<sup>-+</sup></b> | <b>0<sup>+</sup></b> | <b><math>S</math></b> | <b><math>f_2\pi</math></b>  | <b>1.200</b>                    |
| 2 <sup>-+</sup>       | 0 <sup>+</sup>       | $P$                   | $\rho\pi$                   | 0.800                           |
| 2 <sup>-+</sup>       | 0 <sup>+</sup>       | $D$                   | $f_2\pi$                    | 1.500                           |
| 2 <sup>-+</sup>       | 0 <sup>+</sup>       | $D$                   | $(\pi\pi)_{S\pi}$           | 0.800                           |
| 2 <sup>-+</sup>       | 0 <sup>+</sup>       | $F$                   | $\rho\pi$                   | 1.200                           |
| 2 <sup>-+</sup>       | 1 <sup>+</sup>       | $S$                   | $f_2\pi$                    | 1.200                           |
| 2 <sup>-+</sup>       | 1 <sup>+</sup>       | $P$                   | $\rho\pi$                   | 0.800                           |
| 2 <sup>-+</sup>       | 1 <sup>+</sup>       | $D$                   | $f_2\pi$                    | 1.500                           |
| 2 <sup>-+</sup>       | 1 <sup>+</sup>       | $D$                   | $(\pi\pi)_{S\pi}$           | 1.200                           |
| 2 <sup>-+</sup>       | 1 <sup>+</sup>       | $F$                   | $\rho\pi$                   | 1.200                           |
| 2 <sup>++</sup>       | 1 <sup>+</sup>       | $P$                   | $f_2\pi$                    | 1.500                           |
| <b>2<sup>++</sup></b> | <b>1<sup>+</sup></b> | <b><math>D</math></b> | <b><math>\rho\pi</math></b> | <b>—</b>                        |
| 3 <sup>++</sup>       | 0 <sup>+</sup>       | $S$                   | $\rho_3\pi$                 | 1.500                           |
| 3 <sup>++</sup>       | 0 <sup>+</sup>       | $P$                   | $f_2\pi$                    | 1.200                           |
| 3 <sup>++</sup>       | 0 <sup>+</sup>       | $D$                   | $\rho\pi$                   | 1.500                           |
| 3 <sup>++</sup>       | 1 <sup>+</sup>       | $S$                   | $\rho_3\pi$                 | 1.500                           |
| 3 <sup>++</sup>       | 1 <sup>+</sup>       | $P$                   | $f_2\pi$                    | 1.200                           |
| 3 <sup>++</sup>       | 1 <sup>+</sup>       | $D$                   | $\rho\pi$                   | 1.500                           |
| 4 <sup>-+</sup>       | 0 <sup>+</sup>       | $F$                   | $\rho\pi$                   | 1.200                           |
| 4 <sup>-+</sup>       | 1 <sup>+</sup>       | $F$                   | $\rho\pi$                   | 1.200                           |
| 4 <sup>++</sup>       | 1 <sup>+</sup>       | $F$                   | $f_2\pi$                    | 1.600                           |
| <b>4<sup>++</sup></b> | <b>1<sup>+</sup></b> | <b><math>G</math></b> | <b><math>\rho\pi</math></b> | <b>1.640</b>                    |
| 1 <sup>-+</sup>       | 0 <sup>-</sup>       | $P$                   | $\rho\pi$                   | —                               |
| 1 <sup>-+</sup>       | 1 <sup>-</sup>       | $P$                   | $\rho\pi$                   | —                               |
| 1 <sup>++</sup>       | 1 <sup>-</sup>       | $S$                   | $\rho\pi$                   | —                               |
| 2 <sup>-+</sup>       | 1 <sup>-</sup>       | $S$                   | $f_2\pi$                    | 1.200                           |
| 2 <sup>++</sup>       | 0 <sup>-</sup>       | $P$                   | $f_2\pi$                    | 1.300                           |
| 2 <sup>++</sup>       | 0 <sup>-</sup>       | $D$                   | $\rho\pi$                   | —                               |
| 2 <sup>++</sup>       | 1 <sup>-</sup>       | $P$                   | $f_2\pi$                    | 1.300                           |
| Flat                  | —                    | —                     | —                           | —                               |

terms of Breit-Wigner amplitudes:

(7)

$$\rho_{ij}^\epsilon(m_X) = \sum_r \left[ \sum_k^{\text{resonances}} c_{ikr}^\epsilon \text{BW}_k(m_X) \right] \left[ \sum_l^{\text{resonances}} c_{jlr}^\epsilon \text{BW}_l(m_X) \right]^*$$

Here  $\text{BW}_i(m_X)$  is the relativistic Breit-Wigner amplitude for resonance  $i$ :

$$(8) \quad \text{BW}_i(m_X; M_0, \Gamma_0) = \frac{1}{m_X^2 - M_0^2 + i\Gamma_{\text{tot}}(m_X)M_0}$$

where  $\Gamma_{\text{tot}}(m_X) = \sum_n^{N_{\text{decay}}} \Gamma_n(m_X)$  is the total mass-dependent width of the resonance including phase space factors and Blatt-Weisskopf barrier penetration factors  $B_{L_n}(q_n)$  [31] for all  $N_{\text{decay}}$  decay channels:

$$(9) \quad \Gamma_{\text{tot}}(m_X) = \sum_n^{N_{\text{decay}}} \Gamma_{0n} \frac{M_0}{m_X} \frac{q_n}{q_{0n}} \frac{B_{L_n}^2(q_n)}{B_{L_n}^2(q_{0n})}$$

with  $\Gamma_0 = \Gamma_{\text{tot}}(M_0)$ . Here  $q_n$  represents the breakup momentum of the particular two-body decay and  $q_{0n} = q_n(M_0)$ . If required by the data, for some waves an additional coherent exponential background term of the form  $e^{-\alpha q^2}$  was added. The waves selected for the mass-dependent fit exhibit either significant amplitudes or rapid phase motions in the 1.7 GeV/c<sup>2</sup> mass region.

### 3.3 Results

Figure 9 shows the most dominant wave, 1<sup>++</sup>0<sup>+</sup>[ $\rho\pi$ ]S. The data points with statistical error bars are the result of the mass-independent fit. The wave intensity exhibits a broad structure around 1.2 GeV/c<sup>2</sup> which is the  $a_1(1260)$ . The continuous line represents the result of the mass-dependent  $\chi^2$ -fit of the intensities and phase differences of six waves (see Table 1). In this fit the peak is well described using a Breit-Wigner parameterization according to Bowler [35] and a small exponential background which could be caused by the Deck-effect [36].

The second most intense wave is the 2<sup>++</sup>1<sup>+</sup>[ $\rho\pi$ ]D wave which is depicted in Fig. 10. It is also the strongest  $M = 1$  wave and can be large only at high  $t'$ . The sharp peak of the  $a_2(1320)$  is described by a Breit-Wigner, where the mass-dependent total width  $\Gamma_{\text{tot}}(m_X)$  takes into account the two dominant decay modes of the  $a_2(1320)$  to [ $\rho\pi$ ]D and [ $\eta\pi$ ]D with strength according to PDG [32]. In order to reproduce the high-mass tail of the wave and its interference with the 1<sup>++</sup>0<sup>+</sup>[ $\rho\pi$ ]S and the 2<sup>-+</sup>0<sup>+</sup>[ $f_2\pi$ ]S waves, a second Breit-Wigner for the  $a_2(1700)$  with its parameters fixed to the PDG values [32] was added to the fit.

The third significant wave is the 2<sup>-+</sup>0<sup>+</sup>[ $f_2\pi$ ]S wave shown in Fig. 11. A Breit-Wigner corresponding to the  $\pi_2(1670)$  fits the data well. Its total width was parameterized assuming 60 % [ $f_2\pi$ ]S and 40 % [ $\rho\pi$ ]P decays, neglecting contributions below 10 %.

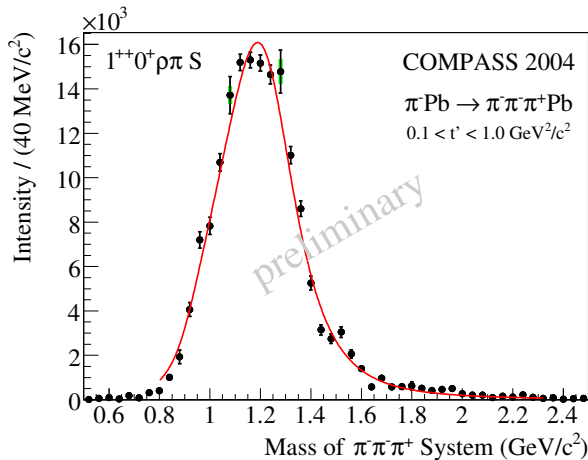
In order to study the sensitivity of the PWA to small signals, two low-intensity waves with known resonances were included in the mass-dependent fit: the 4<sup>++</sup>1<sup>+</sup>[ $\rho\pi$ ]G



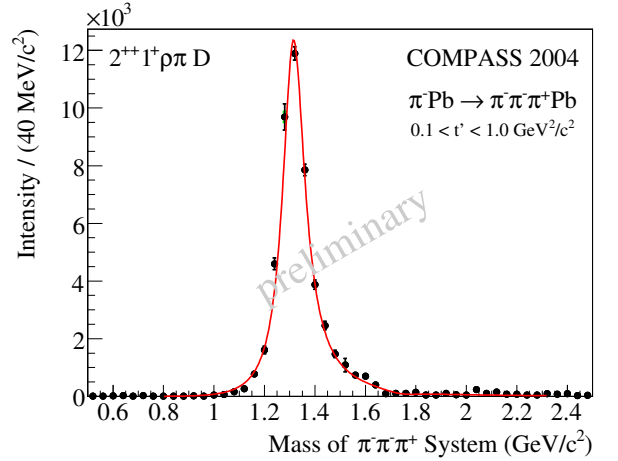
wave with the  $a_4(2040)$  (see Fig. 12) and the  $0^{-+}0^{+}[f_0(980)\pi]S$  wave with the  $\pi(1800)$  (see Fig. 13). The  $4^{++}1^{+}[\rho\pi]G$  wave peaks around  $1.9 \text{ GeV}/c^2$  and is fit by a Breit-Wigner amplitude using a constant width in its denominator, because no branching fractions are known for the  $a_4(2040)$ . The resulting  $a_4$  mass of  $1884 \pm 13(\text{stat.})_{-2}^{+50}(\text{syst.})$  is lower than the PDG average [32], but has a large systematic error. Even fainter in intensity is the  $\pi(1800)$  peak in the  $0^{-+}0^{+}[f_0(980)\pi]S$  wave, but it exhibits a clear phase motion with respect to the  $\pi_2(1670)$  in the  $2^{-+}0^{+}[f_2\pi]S$  wave (not shown here). A Breit-Wigner with constant total width on top of a background describes the data.

Figure 14 shows the intensity of the spin-exotic  $1^{-+}1^{+}[\rho\pi]P$  wave. The distribution exhibits a broad bump at  $1.7 \text{ GeV}/c^2$  and a shoulder at lower masses. The phase difference between this wave and the  $1^{++}0^{+}[\rho\pi]S$  wave, as depicted in Fig. 15, exhibits a rising phase motion around  $1.7 \text{ GeV}/c^2$ , in the tail region of the  $a_1(1260)$ , thus indicating a resonant behavior of the spin-exotic wave. This is supported by the flat phase difference with respect to the  $2^{-+}0^{+}[f_2\pi]S$  wave as shown in Fig. 16 which can be explained by a  $1^{-+}$  resonance with mass and width similar to that of the  $\pi_2(1760)$  which dominates the  $2^{-+}$  wave. The intensity and the phase differences of the  $1^{-+}$  amplitude are fit by a Breit-Wigner with constant total width on top of an exponential background that describes the low-mass shoulder. The extracted resonance parameters of  $M_0 = 1660 \pm 10(\text{stat.})_{-64}^{+0}(\text{syst.}) \text{ MeV}/c^2$  and  $\Gamma_0 = 269 \pm 21(\text{stat.})_{-64}^{+42}(\text{syst.}) \text{ MeV}/c^2$  are in agreement with the disputed  $\pi_1(1600)$ .

Table 2 summarizes the resonance parameters extracted by the mass-dependent fit which are in good agreement with the PDG values [32]. The table also gives the intensities of the resonant part of the particular waves integrated over the mass range from  $0.80$  to  $2.32 \text{ GeV}/c^2$  and normalized to the total intensity of the waves in the mass-dependent fit, which corresponds to  $38.7(2) \%$  of the total acceptance-corrected data sample in the mass range.



**Fig. 9.** Intensity of the  $1^{++}0^{+}[\rho\pi]S$  partial wave. The wave exhibits a broad peak from the  $a_1(1260)$ . The continuous line shows the result of the mass-dependent fit.



**Fig. 10.** Intensity of the  $2^{++}1^{+}[\rho\pi]D$  partial wave. The wave is dominated by a narrow  $a_2(1320)$  peak. The continuous line shows the result of the mass-dependent fit.

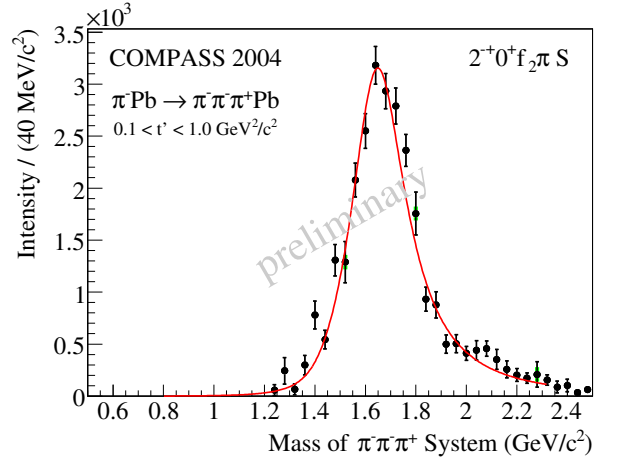


**Fig. 11.** Intensity of the  $2^{-+}0^{+}[f_2\pi]S$  partial wave. The wave exhibits a broad  $\pi_2(1670)$  peak. The continuous line represents the result of the mass-dependent fit.

Several studies were performed to test the stability of the  $1^{-+}$  wave with respect to various assumptions made in the analysis, e.g. by adding and removing waves, varying cuts or initial values of the fit parameters, and shifting the mass binning in the mass-independent fit. In addition the dependence of the fit on the rank  $N_r$  was studied. The fit with  $N_r = 1$  shows an increase of the flat background wave from  $5.8 \%$  for  $N_r = 2$  to  $19 \%$  with respect to the total acceptance-corrected data sample in the mass range from  $0.5$  to  $2.5 \text{ GeV}/c^2$ . For  $N_r = 3$  this value drops to  $1.2 \%$ . This fit, however, exhibits larger bin-to-bin fluctuations. In both cases the  $1^{-+}$  intensity was not significantly altered in the region between  $1.5$  and  $1.8 \text{ GeV}/c^2$ .

In [20] it was shown that an inhomogeneous acceptance not completely taken into account by the Monte Carlo simulation or an incomplete wave set may lead to leakage of intensity of non-exotic waves into the  $1^{-+}1^{+}$  wave. This effect was studied by generating Monte Carlo events using the parameters of the 16 most dominant waves excluding

**Table 2.** Preliminary resonance parameters and intensities of the specified decay channels for the six waves included in the mass-dependent fit. The first uncertainty corresponds to the statistical error, the second one to the systematic error.

| State         | Mass [MeV/c <sup>2</sup> ] | Width [MeV/c <sup>2</sup> ] | Intensity [%]                | Channel $J^{PC} M^{\epsilon}[\text{decay}]L$ |
|---------------|----------------------------|-----------------------------|------------------------------|--|
| $a_1(1260)$   | $1255 \pm 6_{-17}^{+7}$    | $367 \pm 9_{-25}^{+28}$     | $67 \pm 3_{-20}^{+4}$        | $1^{++}0^{+}[\rho\pi]S$                      |
| $a_2(1320)$   | $1321 \pm 1_{-7}^{+0}$     | $110 \pm 2_{-15}^{+2}$      | $19.2 \pm 0.6_{-2.2}^{+0.3}$ | $2^{++}1^{+}[\rho\pi]D$                      |
| $\pi_2(1670)$ | $1658 \pm 3_{-8}^{+24}$    | $271 \pm 9_{-24}^{+22}$     | $10.0 \pm 0.4_{-0.7}^{+0.7}$ | $2^{-+}0^{+}[f_2\pi]S$                       |
| $a_4(2040)$   | $1885 \pm 13_{-2}^{+50}$   | $294 \pm 25_{-19}^{+46}$    | $1.0 \pm 0.3_{-0.1}^{+0.1}$  | $4^{++}1^{+}[\rho\pi]G$                      |
| $\pi(1800)$   | $1785 \pm 9_{-6}^{+12}$    | $208 \pm 22_{-37}^{+21}$    | $0.8 \pm 0.1_{-0.1}^{+0.3}$  | $0^{-+}0^{+}[f_0\pi]F$                       |
| $\pi_1(1600)$ | $1660 \pm 10_{-64}^{+0}$   | $269 \pm 21_{-64}^{+42}$    | $1.7 \pm 0.2_{-0.1}^{+0.9}$  | $1^{-+}1^{+}[\rho\pi]P$                      |

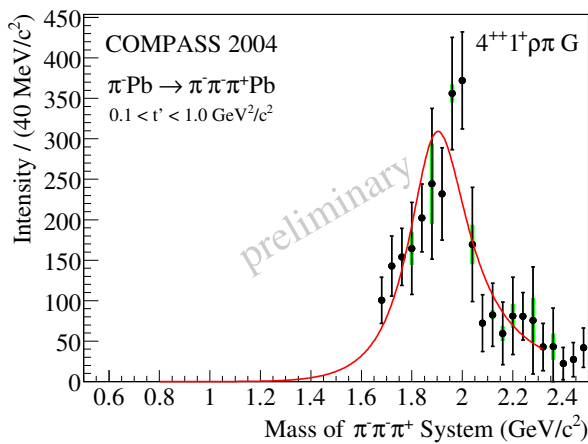


**Fig. 12.** Intensity of the  $4^{++}1^{+}[\rho\pi]G$  partial wave. The broad peak around  $1.9 \text{ GeV}/c^2$  is attributed to the  $a_4(2040)$ . The continuous line shows the result of the mass-dependent fit.

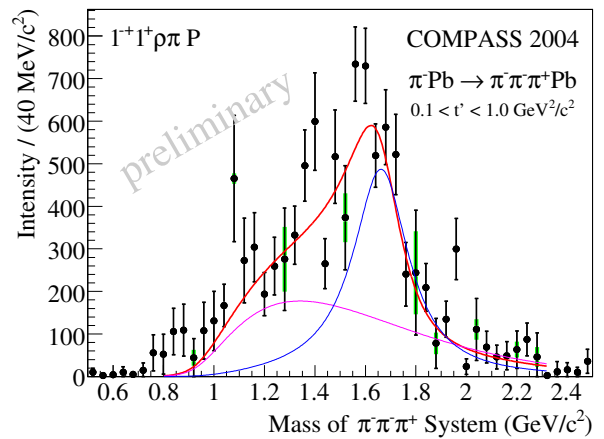


**Fig. 14.** Intensity of the spin-exotic  $1^{-+}1^{+}[\rho\pi]P$  partial wave. The distribution exhibits a broad bump around  $1.7 \text{ GeV}/c^2$ . The red curve shows the result of the mass-dependent fit with one Breit-Wigner for the  $\pi_1(1600)$  (blue curve) on top of a background (purple curve).

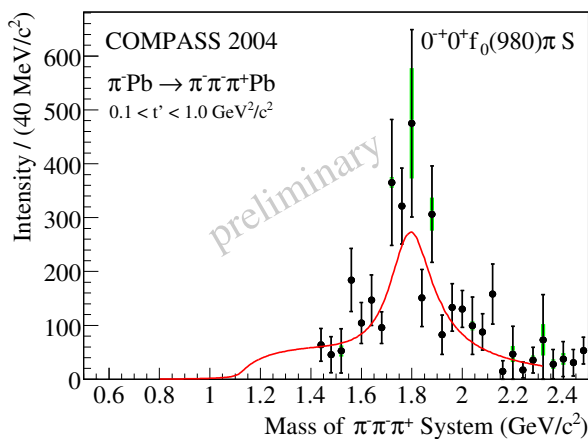


**Fig. 13.** Intensity of the  $0^{-+}0^{+}[f_0(980)\pi]S$  partial wave. The structure around  $1.8 \text{ GeV}/c^2$  is attributed to the  $\pi(1800)$ . The continuous line shows the result of the mass-dependent fit.

the  $1^{-+}$  wave. The Monte Carlo data were then processed by the same PWA used for the real data. The amount of

intensity leaking from the 16 major waves into the  $1^{-+}1^{+}[\rho\pi]P$  wave was found to be below 5 % of the  $1^{-+}$  intensity and is therefore negligible. This is mainly due to the flat angular acceptance and the better resolution of COMPASS, both well reproduced by the simulations.

In the mass-dependent fit the low mass shoulder in the  $1^{-+}1^{+}[\rho\pi]P$  wave is accounted for by a non-resonant exponential background, which is possibly caused by a Deck-like effect [36]. In an alternative attempt to describe the shoulder the additional Breit-Wigner for the  $\pi_1(1400)$  with its parameters fixed to the PDG values [32] was included in the mass-dependent fit. This did not significantly alter the intensity or the phase difference of any of the waves in the mass-dependent fit, but slightly shifted the  $\pi_1(1600)$  towards smaller masses which was included in the systematic error.

Also using different parameterizations for the  $\pi\pi$   $S$ -wave and the  $\rho(770)$  and replacing the Zemach tensors by rotation functions with relativistic corrections [37] did not significantly change the result. This is also true for tests,



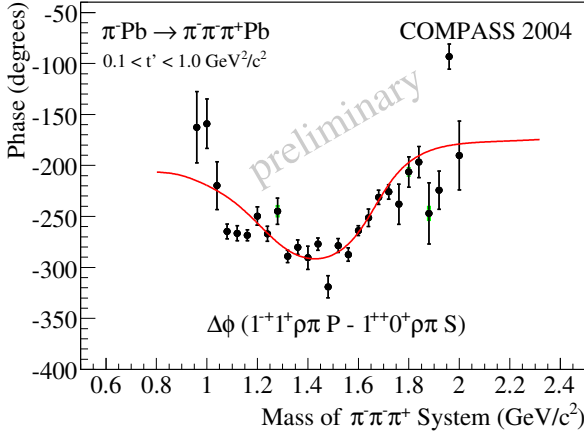


**Fig. 15.** Phase difference of the  $1^{-+}1^{+}[\rho\pi]P$  and the  $1^{++}0^{+}[\rho\pi]S$  partial waves. A clear phase motion is seen in the region around  $1.7 \text{ GeV}/c^2$  which can be explained by a  $\pi_1(1600)$  resonance interfering with the tail of the  $a_1(1260)$ . The continuous line shows the result of the mass-dependent fit.

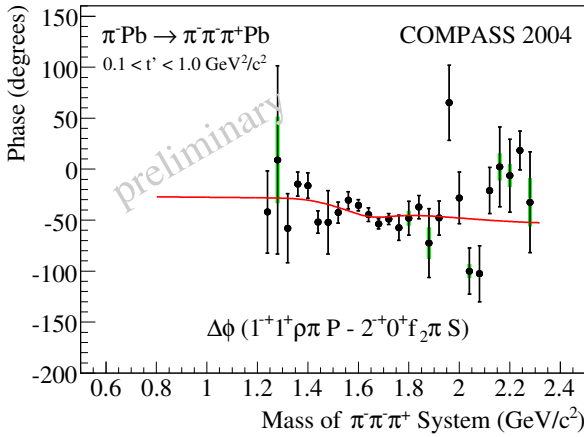


**Fig. 16.** Phase difference of the  $1^{-+}1^{+}[\rho\pi]P$  and the  $2^{-+}0^{+}[f_2\pi]S$  partial waves. The phase difference is virtually flat which can be explained by a  $\pi_1(1600)$  resonance with resonance parameters similar to the  $\pi_2(1670)$ . The continuous line shows the result of the mass-dependent fit.

where the PWA was performed without the  $t'$ -dependent factors in the partial-wave amplitudes.

It cannot be ruled out, however, that the  $\pi_1(1600)$  signal is an artifact of the simplifying assumptions made in the PWA model. Final state interactions in particular the Deck-mechanism were found to be relevant in the  $\pi^{-}\pi^{+}\pi^{-}$  system [38,39] and might cause spurious signals.

### 3.4 Run 2008/9 Data

The analysis of the data from the 2004 pilot run marked only the beginning of the hadron spectroscopy program at COMPASS. During the years 2008 and 2009 COMPASS collected very large diffractive and central production data sets using  $190 \text{ GeV}/c$  positive and negative hadron beams

mostly on liquid hydrogen targets. These data will make it possible to study a number of channels with unprecedented precision.

Several analyses have started: Figure 17 shows the  $\pi^{-}\pi^{+}\pi^{-}$  invariant mass spectrum after event selection. The tremendous boost in statistics will enable COMPASS to extract precise resonance parameters, to study the  $t'$ -dependence of resonance production, and to hopefully settle the  $\pi_1(1600)$  issue in the diffractive  $\pi^{-}\pi^{+}\pi^{-}$  channel. This analysis will be accompanied by a PWA of the  $\pi^{-}\pi^{0}\pi^{0}$  final state which will provide important internal cross checks of our results. Furthermore the PWA will be extended to the region of  $t' < 0.1 \text{ (GeV}/c^2)^2$ . Data sets with different targets will give access to possible nuclear effects in diffractive production.

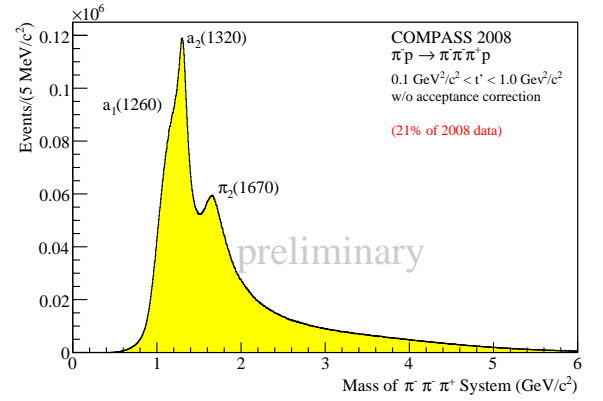


**Fig. 17.** Invariant mass distribution  $\pi^{-}\pi^{+}\pi^{-}$  final states diffractively produced by a  $\pi^{-}$  beam on a liquid hydrogen target; based on 21 % of the 2008 data set.

In addition COMPASS will search for scalar and tensor glueballs in centrally produced  $\pi^{+}\pi^{-}\pi^{+}\pi^{-}$  systems. Figure 18 depicts the  $\pi^{+}\pi^{-}\pi^{+}\pi^{-}$  invariant mass with and without selecting centrally produced event via the cut  $x_F(\pi_{\text{fast}}^{-}) > 0.7$ . A clear signal from the  $f_1(1285)$  is seen.

The  $f_1\pi$  and maybe even the  $b_1\pi$  channel, into which the  $1^{-+}$  hybrid is predicted to preferentially decay, can also be studied in charged five pion final states produced in  $\pi A \rightarrow \pi^{-}\pi^{+}\pi^{-}\pi^{+}\pi^{-}A$ . Furthermore this channel gives access to higher masses above  $2 \text{ GeV}/c^2$ , where the PDG lists many states that need confirmation [32].

Finally COMPASS will search for possible hybrids and glueballs in kaonic final states produced in reactions like  $\pi^{-}p \rightarrow \pi^{-}K^{+}K^{-}p$ ,  $\pi^{-}K_S^0 K_S^0 p$ , or  $\pi^{-}K_S^0 K_L^0 p$ . Moreover the CEDAR detectors enable COMPASS to measure diffraction of kaon beam, e.g. in  $K^{-}p \rightarrow K^{-}\pi^{+}\pi^{-}p$ .

## 4 Summary

COMPASS has started its hadron spectroscopy program with the main goal to precisely explore the light-meson sector in order to search for states with gluonic degrees of freedom like hybrids and glueballs and to settle the properties of controversial states like the  $\pi_1(1400)$ ,  $\pi_1(1600)$ , and

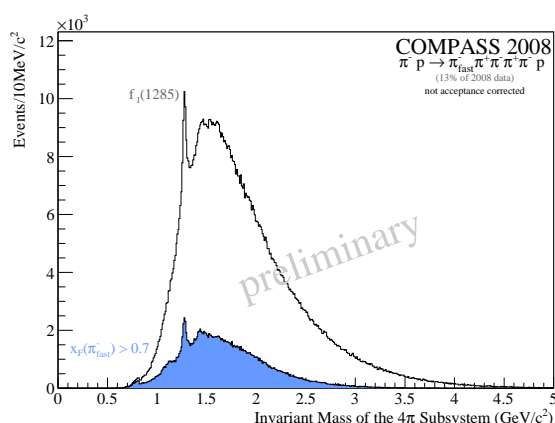


**Fig. 18.** Invariant mass distribution of the  $\pi^+\pi^-\pi^+\pi^-$  system produced in  $\pi^- p \rightarrow \pi_{\text{fast}}^-(\pi^+\pi^-\pi^+\pi^-)p_{\text{recoil}}$  with and without the cut  $x_F(\pi_{\text{fast}}^-) > 0.7$ ; based on 13 % of the 2008 data set.

the  $f_0(1500)$ . At COMPASS two production mechanisms, diffractive dissociation and central production, can be measured in parallel using  $\pi$ ,  $K$ , or  $p$  beams. The spectrometer provides high acceptance and excellent resolution for final states containing both charged and neutral particles.

In a short first pilot run in 2004 COMPASS acquired a diffractive data set using a 190 GeV/c  $\pi^-$  beam scattered off a lead target. A partial wave analysis of the  $\pi^-\pi^+\pi^-$  final state in the region of  $t' \in [0.1, 1.0]$  (GeV/c)<sup>2</sup> shows several of the well-known resonances expected in this channel. In addition we observe a spin-exotic  $J^{PC} = 1^{-+}$  state with significant intensity in the  $\rho\pi$  decay channel in natural parity exchange at a mass of 1.66 GeV/c<sup>2</sup>. The mass dependence of its phase and its resonance parameters are consistent with the disputed  $\pi_1(1600)$ .

Based on the experience of the pilot run the spectrometer was upgraded and improved. In particular a detector to measure the target recoil was added to the setup. During dedicated runs in 2008 and 2009 COMPASS accumulated diffractive and central production data sets of unprecedented statistics using 190 GeV/c hadron beams. The bulk of the data were taken with a liquid hydrogen target, but also nickel, tungsten, and lead targets were measured. First analyses of diffractive and central production reactions have started.

This work is supported by the the German Bundesministerium für Bildung und Forschung, the Maier-Leibnitz-Labor der LMU und TU München, the DFG Cluster of Excellence *Origin and Structure of the Universe*, and CERN-RFBR grant 08-02-91009.

## References

1. E. Klempt and A. Zaitsev, Phys. Rept. **454** (2007) 1
2. Y. Chen *et al.*, Phys. Rev. **D73** (2006) 014516
3. C. Amsler *et al.*, Phys. Lett. **B353** (1995) 571
4. D. Barberis *et al.*, Phys. Lett. **B474** (2000) 423
5. K.J. Juge, J. Kuti, and C. Morningstar, AIP Conf. Proc. **688** (2004) 193

6. F.E. Close and P.R. Page, Nucl. Phys. **B443** (1995) 233
7. D.R. Thompson *et al.*, Phys. Rev. Lett. **79** (1997) 1630
8. V. Dorofeev *et al.*, AIP Conf. Proc. **619** (2002) 143
9. A. Abele *et al.*, Phys. Lett. **B423** (1998) 175
10. A. Abele *et al.*, Phys. Lett. **B446** (1999) 349
11. G.S. Adams *et al.*, Phys. Rev. Lett. **81** (1998) 5760
12. S.U. Chung *et al.*, Phys. Rev. **D65** (2002) 072001
13. Yu.A. Khokhlov *et al.*, Nucl. Phys. **A663** (2000) 596
14. E.I. Ivanov *et al.*, Phys. Rev. Lett. **86** (2001) 3977
15. G.M. Beladidze *et al.*, Phys. Lett. **B313** (1993) 276
16. J. Kuhn *et al.*, Phys. Lett. **B595** (2004) 109
17. D.V. Amelin *et al.*, Phys. Atom. Nucl. **68** (2005) 359
18. M. Lu *et al.*, Phys. Rev. Lett. **94** (2005) 032002
19. C.A. Baker *et al.*, Phys. Lett. **B563** (2003) 140
20. A.R. Dzierba *et al.*, Phys. Rev. **D73** (2006) 072001
21. U. Amaldi, M. Jacob, and G. Matthiae, Ann. Rev. Nucl. Part. Sci. **26** (1976) 385
22. P. Abbon *et al.*, Nucl. Instrum. Meth. **A577** (2007) 455
23. Q. Weitzel, Int. J. Mod. Phys. **A24** (2009) 484
24. Q. Weitzel, Ph.D. Thesis, TU München, Physik-Department E18 (2008)
25. M. Alekseev *et al.*, submitted to Phys. Rev. Lett. (2009)
26. S.U. Chung and T.L. Trueman, Phys. Rev. **D11** (1975) 633
27. C. Zemach, Phys. Rev. **B97** (1965) 140; *ibid.* **B109** (1965) 140
28. S.U. Chung, CERN-71-08, Lectures given in the Academic Training Program of CERN (1971)
29. K. Gottfried and J.D. Jackson, Nuovo Cimento **33** (1964) 309
30. G. Ascoli *et al.*, Phys. Rev. Lett. **25** (1970) 962
31. F. von Hippel and C. Quigg, Phys. Rev. **D5** (1972) 624
32. W.M. Yao *et al.*, J. Phys. **G33** (2006) 1
33. D.V. Amelin *et al.*, Phys. Lett. **B356** (1995) 595
34. K.L. Au, D. Morgan, M.R. Pennington, Phys. Rev. **D35** (1987) 1633
35. M.G. Bowler, Phys. Lett. **B209** (1988) 99
36. R.T. Deck, Phys. Rev. Lett. **13** (1964) 169
37. S.U. Chung and J. Friedrich, Phys. Rev. **D78** (2008) 074027
38. G. Ascoli, L.M. Jones, B. Weinstein, and H.W. Wyld, Phys. Rev. **D8** (1973) 3894
39. G. Ascoli, R. Cutler, L.M. Jones, U. Kruse, T. Roberts, B. Weinstein, and H.W. Wyld, Phys. Rev. **D9** (1974) 1963